IEEE Access
Multidisciplinary ⋮ Rapid Review ⋮ Open Access Journal

Received 23 October 2023, accepted 19 November 2023, date of publication 27 November 2023,
date of current version 5 December 2023.

Digital Object Identifier 10.1109/ACCESS.2023.3337050

RESEARCH ARTICLE

Dynamic Blockage in Indoor Reflection-Aided Sub-Terahertz Wireless Communications

ALEXANDER SHURAKOV[1,2], POLINA ROZHKOVA[2], ABDUKODIR KHAKIMOV[3], EVGENY MOKROV[3], ANATOLIY PRIKHODKO[1,2,4], VYACHESLAV BEGISHEV[3], YEVGENI KOUCHERYAVY[1], MIKHAIL KOMAROV[1], (Senior Member, IEEE), AND GREGORY GOL'TSMAN[1,2,4]

[1]HSE University, 101000 Moscow, Russia
[2]Department of General and Experimental Physics, Moscow Pedagogical State University, 119991 Moscow, Russia
[3]Department of Probability Theory and Cyber Security, Peoples' Friendship University of Russia (RUDN University), 117198 Moscow, Russia
[4]Russian Quantum Center, 121205 Skolkovo, Russia

Corresponding author: Alexander Shurakov (alexander@rplab.ru)

This work was supported in part by the Russian Science Foundation under Grant 21-79-10139 https://rscf.ru/en/project/21-79-10139/ (Sections I, II) and Grant 22-79-10279 https://rscf.ru/project/22-79-10279/ (Sections III, IV); in part by the Strategic Project "Digital Transformation: Technologies, Effectiveness, Efficiency" of Higher School of Economics Development Programme granted by the Ministry of Science and Higher Education of Russia under Grant "Priority-2030" as a part of the "Science and Universities" National Project (Sections V–VII); and in part by the Basic Research Program of the National Research University Higher School of Economics.

ABSTRACT The sixth-generation cellular systems are expected to utilize the sub-terahertz frequency band covering $100-300$-GHz. Due to high path losses, the coverage of such systems will be limited to a few tens of meters making them suitable for indoor environments. As compared to outdoor deployments, indoor usage of sub-terahertz systems is characterized by the need to operate over shorter distances using both line-of-sight (LoS) and in-reflection propagation paths. This potentially results not only in the attenuation of radio signal, but in the appearance of diffraction signatures in its time-related metrics too. We conduct a detailed measurement campaign at the carrier frequency of 156 GHz and report on the dynamics of the reflection and blockage losses as well as signal fall, blockage, and recovery times over various in-reflection paths. We also develop reflection model and use it to extract the complex permittivities of glass, drywall and aerated concrete from their measured reflection spectra. The extracted permittivities of $7.23+0.22i$, $2.63+0.026i$, $1.9+0.017i$ are consistent with the material-dependent reflection losses, which are as high as 16 dB for transverse electric (TE)-polarized and 39 dB for transverse magnetic (TM)-polarized signals. Moreover, the asymmetry in the side lobe levels of the transmitting and receiving antenna beams results in the additional losses ranging from 16 to 49 dB as measured for 3.55–4.3-m long non-specular paths with the angles of departure and reception within $30-70°$. The blockage losses, in turn, are in the range of $6-17$ dB. We observe that the presence of a re-directing material does not affect their mean value. However, the acquired blockage duration, signal fall and recovery times are noticeably smaller than in the LoS channels with the same directivity. This implies that the time-budget for blockage detection is much smaller: it reduces to just 20–40 ms as compared to 80–100 ms intrinsic to the LoS propagation paths.

INDEX TERMS 6G, sub-terahertz, indoor, reflection, permittivity, dynamic blockage.

I. INTRODUCTION

Seeking for the capacity boost at the access interface in cellular systems, ITU-R and 3GPP employ the millimeter wave (mmWave) band covering $30-100$ GHz for 5G New Radio (NR) systems [1]. The next step in the evolution of such systems is the utilization of the sub-terahertz frequency band (sub-THz, $100-300$ GHz), where large parts of the spectrum are still not regulated and tens of gigahertz of bandwidth can be allocated to 6G systems [2].

The associate editor coordinating the review of this manuscript and approving it for publication was Bilal Khawaja.

To partially compensate for the effective antenna aperture that reduces with the increase of the carrier frequency, similarly to 5G NR mmWave systems, 6G sub-THz systems will heavily rely on the use of antenna arrays at both base station (BS) and user equipment (UE) operating in beamforming mode. Nevertheless, the coverage of such systems will still be limited to tens or hundreds of meters making them a suitable choice for indoor areas, where most of the traffic demands originate. The landscape of applications in the indoor environment is rather large including conventional 4k/8k video watching, virtual/augmented reality (AR/VR) gaming, and forthcoming applications such as collective VR gaming, holographic communications [3], etc.

Indoor deployments of 6G sub-THz systems are characterized by several propagation specifics. First of all, the link distances are on average smaller as compared to those outdoors. Secondly, due to rather small heights of BS, human body blockage is more likely to occur. Finally, as a result of the complex geometry of indoor premises, communications over the non-line-of-sight (NLoS) paths with reflections of radio signal are expected to be much more common. Specifically, short distances have been recently shown to lead to much smaller human body blockage attenuation at 156 GHz varying in the range of $8-13$ dB [4] as compared to $15-35$ dB losses over larger distances and at lower frequencies, e.g., as reported in [5] and [6].

The aim of this paper is to characterize the impact of dynamic human body blockage over in-reflection propagation paths on the signal strength in a highly directive sub-THz channel for typical indoor scenarios. By carrying out a large-scale measurement campaign at the carrier frequency of 156 GHz, we study reflection and blockage losses over various NLoS paths as well as the corresponding blockage duration, signal fall and recovery times. The empirical studies are justified by the material-dependent simulations of the propagation of a 156 GHz radio signal for 24 different measurements configurations.

The main findings of our paper acquired empirically are:

- the complex permittivities of flat glass, drywall and aerated concrete are equal to $7.23+0.22i$, $2.63+0.026i$, $1.9+0.017i$, respectively;
- the reflection losses reach 16 dB for transverse electric (TE)-polarized and 39 dB for transverse magnetic (TM)-polarized radio signals;
- the path losses due to the asymmetry in the side lobe levels of the transmitter (Tx) and receiver (Rx) antenna beams with 6° wide symmetric main lobes vary from 16 to 49 dB as measured for 3.55–4.3 m long non-specular NLoS paths for the angles of departure (AoD) and reception (AoR) within $30-70°$;
- the blockage losses are in the range of $6-17$ dB, and their mean value is nearly unaffected by the change of a re-directing material in the propagation path;
- the blockage duration, signal fall and recovery times are noticeably smaller than in the line-of-sight (LoS) channels with the same directivity, and the time-budget for blockage detection is 20–40 ms, i.e., 2–4 times as small as compared to the LoS propagation paths.

The paper is organized as follows. First, in Section II, we overview related studies reported in the literature. Next, in Section III, we outline the experimental setup and utilized measurements methodology. Then, in Section IV, we introduce the reflection model. The blockage attenuation statistics are characterized and discussed in Section V. The associated timings related to the blockage duration, signal fall and recovery times are provided in Section VI. Conclusions are given in the last section.

II. RELATED WORK

In this section, we outline related works. We start by briefly reminding the results for the LoS path propagation and blockage. They are recapitulated for comparison purposes in our study. Then, we discuss results similar to those reported in our study which are related to reflection losses and blockage for the NLoS propagation paths in the mmWave and sub-THz bands.

A. LoS PATHS CHARACTERIZATION

In spite of several studies already reporting propagation specifics at frequencies above 100 GHz, the results on blockage process dynamics are still scarce. The study in [7] provided an overview of propagation and penetration loss measurements at 140 GHz for various building materials and beamwidths of 8°. However, the authors did not report blockage process characteristics. The authors in [8] and [9] explicitly reported the attenuation values for a carrier frequency of 300 GHz for vehicular blockage. However, these results cannot be extrapolated to the human body blockage in the indoor environment.

Several authors investigated the transparency properties of the materials [7], [10], [11]. The paper [7] studied the penetration and fall of the signal level for different materials in the sub-THz band, more precisely, for a frequency of 140 GHz. Blockage measurements were made for the following materials: clear glass, glass door, drywall, and drywall with whiteboards of different thicknesses. The drop in the signal strength in the case of drywall with whiteboards blockage was 16.69 dB, while for a glass with a thickness of 0.6 cm – 8.24 dB. In [10], the authors carried out measurements at four different frequencies, two of which belong to the sub-THz band. The configuration of the experimental setup had the following properties: antenna gain is 21 dBi, beamwidth is 15°, and the Tx-to-Rx distance is from 0.2 to 0.7 m. The signal attenuation for the plywood material was reported to be 16.06 dB. Similar results have been reported in [11].

In addition to the studies covering the properties of materials, several authors developed analytical models by accounting for key features of blockage in the sub-THz band. Specifically, the authors in [12], based on the average value of blockage probability estimated empirically as a function of

the mutual arrangement of Rx and Tx, average Tx/Rx heights, antenna parameters, and room dimensions, calculated the average number of people in the room. Then, they proceeded to study the performance improvements in terms of coverage due to the utilization of more than a single antenna. The study in [13] investigated the optimal Tx locations in the room crowded with human blockers to maximize the probability of coverage for a given threshold of signal-to-interference and noise ratio (SINR). For dynamic human body blockage caused by human movement in three-dimensional space, [14] offers a flexible analytical framework to estimate the optimal BS locations in outdoor deployments. The authors highlighted that that the increase in the directivity of the antennas at the BS results in better coverage as compared to increasing the UE directivity. The study in [15] reported on the fraction of time in outage and capacity in the presence of both blockage and user micromobility impairments.

As one of the paper's goals is to compare blockage statistics over NLoS paths to that over LoS paths, we briefly introduce the latter as reported in [4]. Specifically, it has been shown that that the mean attenuation caused by human body blockage varies within $8-13$ dB and is generally independent of blocker-to-Rx and Tx-to-Rx distances. Furthermore, both signal fall and recovery times increase as a function of the distance potentially making it more feasible to detect blockage events timely. The absolute difference between the reported times is insignificant and lies within $2-4\%$ of the nominal values of around 60, 80 and 100 ms for Tx-to-Rx distances of 3, 5 and 7 m, respectively. It is worth noting that both fall and recovery times have almost identical nominal values, and, in general, the recovery time is $7-10\%$ smaller than the fall time.

By summarizing the current state of blockage characterization and modeling, we can see that this effect is going to play a critical role in future 6G sub-THz communication systems. By extrapolating the data available on the penetration of sub-THz signal through various materials and measurement campaigns for vehicular communication, one may expect that the attenuation might be stronger as compared to mmWave band. However, there is still no rigorous characterization of the human body blockage process in the sub-THz band.

B. NLoS PATHS CHARACTERIZATION

The attenuation caused by reflections from different materials was the subject of just a few studies. In [16], the authors reported the measurement results of the received signal diffusely scattered from aluminum, glass, plastic, hardboard, and concrete using terahertz time-domain spectroscopy (THz-TDS) equipment for different angles of incidence. The time duration of utilized pulses was chosen such that the energy is mainly concentrated in the $0.1-4$ THz band. The observed losses were in the range of $10-60$ dB depending on the angle of incidence and type of the material. Specifically, in the $0.1-0.3$ THz band, aluminum demonstrated the least attenuation of around 25–35 dB for the angle of incidence of $\pi/4$.

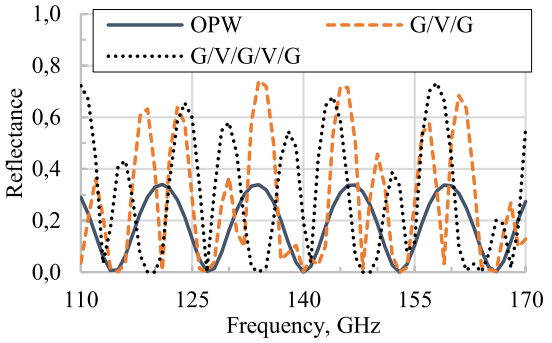

(a) Reflection spectrum.

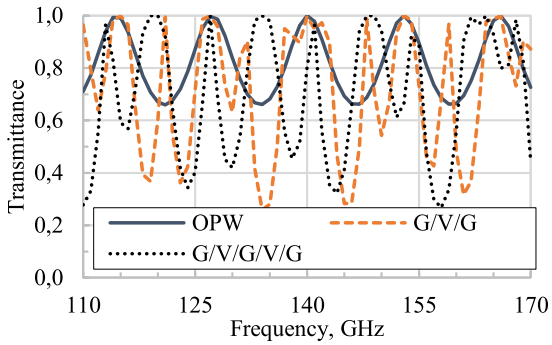

(b) Transmission spectrum.

FIGURE 1. Simulated spectra of constructional flat glass elements.

The authors in [8] and [9] reported the results of reflections from typical vehicle materials at 300 GHz for different configurations including front and rear reflections, side-lane, and under-vehicle reflections. The front and rear reflections were reported to result in 24–42 dB and 15–30 dB attenuation, respectively, while side-lane reflections led to 16–20 dB losses. The authors also proposed to model the under-vehicle reflection losses of the asphalt by utilizing the $\alpha d^{-\beta}$ function, where d is the separation distances, while α and β are some coefficients tabulated in [8].

Similar studies have been performed in the mmWave band. In [17], the authors investigated the impact of polarization properties of the indoor 38 GHz channel after single bounce reflection for different angles of incidence and observation and two types of materials: aluminum and concrete. They highlighted that, when the polarization of Tx and Rx antennas coincide, much smaller losses are experienced. The difference can reach 15–20 dB and is maximized for specular reflections. Concrete results in 8–12 dB higher losses as compared to aluminum.

III. METHODOLOGY OF EMPIRICAL STUDIES

In this section, we first describe our measurements methodology and experimental setup. Then, we detail the scenarios of interest.

A. CHOICE OF CARRIER FREQUENCY

In our empirical studies, we focus on the measurements of in-reflection signal strengths that could be expected for

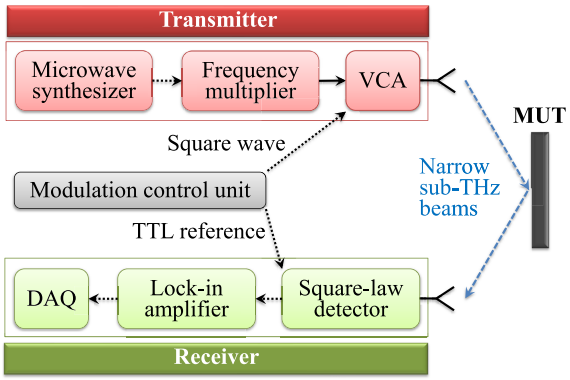

FIGURE 2. Measurement setup diagram.

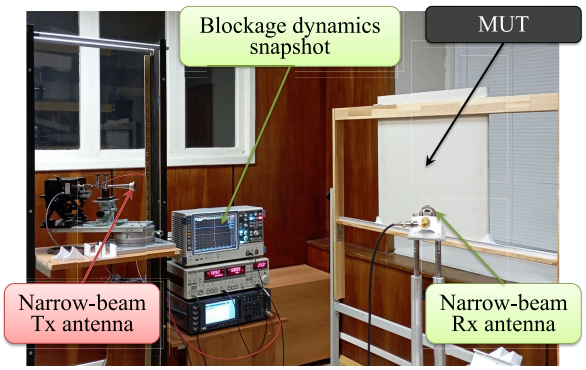

FIGURE 3. Measurement setup photograph.

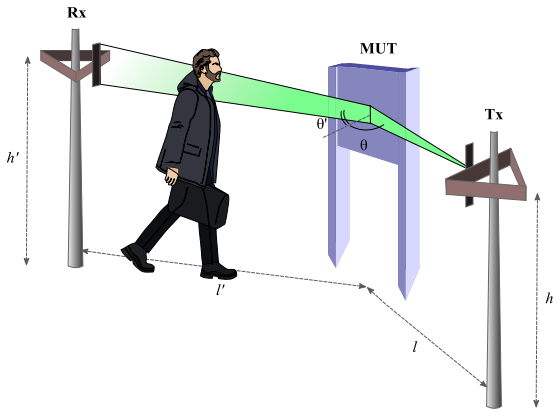

FIGURE 4. Illustration of the considered scenarios.

ultra-directive radio access in typical indoor environments. Given that in modern buildings glass is not only used to implement the outer parts but to separate the inner workplaces as well, we first simulate the impact of a 6 mm thick plate glass elements potentially suitable for multi-chamber windows and office partition walls. Transmission and reflection spectra are preliminary acquired with the aid of a characteristic matrix of a layered dielectric medium [18]. This technique is detailed further in Section IV. The calculations are performed for the normal incidence of a sub-THz wave, and the glass layers are simulated as lossless media with relative permittivity of 3.8. These properties are consistent with those reported in the literature for silicate glasses over the considered frequency range of 110–170 GHz [19], [20]. Referring to Fig. 1, we evaluate typical single-chamber (Glass/Vacuum/Glass) and dual-chamber (Glass/Vacuum/Glass/Vacuum/Glass) window designs, including composition formulas 6/16/6 mm and 6/10/6/10/6 mm. The figure also provides spectra of the office partition wall (OPW) made of a 6 mm thick plate glass. As one can clearly see, the provided spectra differ noticeably. This feature enables the selection of the carrier frequency in a wireless channel such that the transmitted signal efficiently penetrates the inner glass elements in the office and is sufficiently reflected by its outer glass elements. Following this basic idea and taking into account the performance of our sub-THz transmitter, we fix its operating frequency to 156 GHz in all the measurements. The chosen frequency also ensures optimum atmospheric absorption for both low and high humidity environments [21].

B. EXPERIMENTAL SETUP

Referring to Fig. 2, the sub-THz transmitter relies on a microwave synthesizer acting as a fundamental frequency source. The synthesizer is loaded by a wideband frequency multiplier, and the assembly provides up to 120 mW of output power in a continuous wave (CW) regime over 132–162 GHz. The voltage-controllable attenuator (VCA) equipped with a pyramidal horn antenna is employed for modulating the generated CW signal and for creating the sub-THz beam of a few degrees wide. The transmitted beam carrying 44 mW of power is coupled to the pyramidal horn antenna of a sub-THz receiver upon reflection from the surface of a material under test (MUT). The amount of reflected power is registered by a square-law detector whose response voltage is measured by a lock-in amplifier. The amplifier readings are synchronized with the VCA states by a modulation control unit at 25 kHz. The response voltage as a function of time is logged by a data acquisition system (DAQ) and converted into the signal strength at Rx through the detector responsivity, which is equal to 100 V/W at the chosen carrier frequency of 156 GHz. It is worth noting that we account for the total insertion losses of the waveguide components in between of the multiplier and the detector while providing the amount of power in the sub-THz beam.

Fig. 3 provides a photograph of the measurement equipment used in the experiments.

C. SCENARIOS UNDER STUDY

A visual illustration of the considered scenarios is shown in Fig. 4 while Table 1 provides further details on the mutual arrangement of Tx, Rx, MUT and a blocker.

In our studies, we focus on the impact of a blocker passing through the transmitted sub-THz beam at the midpoint between MUT and Rx, i.e., after its reflection from the MUT surface. The overall Tx-to-blocker optical path $d = l + 0.5l'$. Both specular and non-specular receptions are considered

TABLE 1. Experimental setup configurations.

№	P	h, m	h', m	x, m	l, m	l', m	θ, °	θ′, °
1	TM	1.65	1.65	3.00	1.50	1.5	70	70
2	TM	1.65	1.65	4.30	2.80	1.5	50	70
3	TM	1.65	1.65	3.55	2.05	1.5	30	70
4	TM	1.65	1.65	3.00	1.50	1.5	50	50
5	TM	1.65	1.65	3.55	2.05	1.5	30	50
6	TM	1.65	1.65	3.00	1.50	1.5	30	30
7	TM	1.45	1.45	3.00	1.50	1.5	70	70
8	TM	1.45	1.45	4.30	2.80	1.5	50	70
9	TM	1.45	1.45	3.55	2.05	1.5	30	70
10	TM	1.45	1.45	3.00	1.50	1.5	50	50
11	TM	1.45	1.45	3.55	2.05	1.5	30	50
12	TM	1.45	1.45	3.00	1.50	1.5	30	30
13	TE	1.65	1.65	3.00	1.50	1.5	70	70
14	TE	1.65	1.65	4.30	2.80	1.5	50	70
15	TE	1.65	1.65	3.55	2.05	1.5	30	70
16	TE	1.65	1.65	3.00	1.50	1.5	50	50
17	TE	1.65	1.65	3.55	2.05	1.5	30	50
18	TE	1.65	1.65	3.00	1.50	1.5	30	30
19	TE	1.45	1.45	3.00	1.50	1.5	70	70
20	TE	1.45	1.45	4.30	2.80	1.5	50	70
21	TE	1.45	1.45	3.55	2.05	1.5	30	70
22	TE	1.45	1.45	3.00	1.50	1.5	50	50
23	TE	1.45	1.45	3.55	2.05	1.5	30	50
24	TE	1.45	1.45	3.00	1.50	1.5	30	30

Here P denotes the orientation of the polarization plane of Tx-generated wave with respect to the horizontally oriented plane of incidence, h and h' are the vertical positions of Tx and Rx relative to the floor, x is the optical path between Tx and Rx, l is the distance between Tx and MUT, l' is the distance between MUT and Rx, θ is the angle of incidence of the Tx-generated wave on MUT (i.e., AoD), θ′ is the Rx angle of view with respect to the normal to MUT (i.e., AoR).

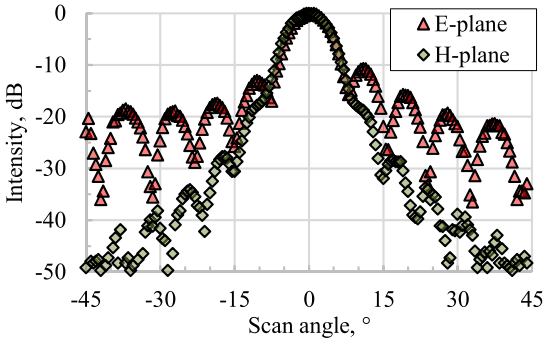

FIGURE 5. Tx/Rx radiation pattern measured at 156 GHz. The profiles are normalized, the Tx/Rx antenna gain $G_a = 28.4$ dBi.

for the Tx/Rx heights corresponding to the blocker head and chest levels. Given that the measured far-field radiation patterns of Tx and Rx have pronounced asymmetry in E- and H-planes as shown in Fig. 5, we also evaluate polarization-dependent effects. This is done for the Tx and Rx polarization planes oriented either horizontally (TM wave) or vertically (TE wave). It is also worth noting that the Tx-Rx LoS is parallel to the MUT plane in all the experimental setup configurations.

IV. REFLECTION MODEL AND MUT PROPERTIES

We choose aerated concrete, drywall, and flat glass as MUT samples to assess reflective properties of constructional materials widely used in modern buildings. It is natural to assume that, in addition to their linear dimensions, the chosen samples notably differ in surface roughness and uniformity, as well as in their dielectric properties. Thus, a proper reflection model is required to justify the relevance of empirically acquired data. The simplest way to predict the reflective properties of the interface between a vacuum and a dielectric medium is to use Fresnel's equations. However, they define reflectance as a physical quantity determined by the angle of incidence of an EM wave and the refractive index of the half-space facing it. This simplification is acceptable only for extremely thick and lossy dielectrics. Given that the studied MUT samples have thicknesses ranging from 6 to 50 mm, the applicability of Fresnel's equations for analysis of all empirically acquired data seems doubtful. For instance, it is natural to expect multiple reflections from the front and rare surfaces of the flat glass sample potentially resulting in pronounced frequency dependence of its reflectance due to interference effects. These effects, in turn, can be accounted for if the reflection spectrum is calculated with the aid of a characteristic matrix of a layered dielectric medium, M [18]:

$$M = \prod_{j=1}^{N} M_j, \text{ where}$$

$$M_j = \begin{bmatrix} \cos(k_0 n_j z_j \cos(\theta_j)) & -\frac{i}{p_j}\sin(k_0 n_j z_j \cos(\theta_j)) \\ -i p_j \sin(k_0 n_j z_j \cos(\theta_j)) & \cos(k_0 n_j z_j \cos(\theta_j)) \end{bmatrix}$$

$$k_0 = \frac{2\pi f}{c},\ n_j = \sqrt{\epsilon_j \mu_j},\ p_j = \sqrt[0.5\,q]{\frac{\epsilon_j}{\mu_j}}\cos(\theta_j),$$

where f is the frequency, c is the speed of light in vacuum, ϵ_j, μ_j and z_j are the relative permittivity, the permeability and the thickness of the j-th layer, and θ_j is the angle of incidence at the j-th layer, N is the total number of layers, q is the constant factor equal to 1 for TE and –1 for TM incident waves.

Using the characteristic matrix technique, one can calculate both reflection and transmission coefficients for a given frequency f as [18]

$$r = \frac{(M_{11} + M_{12} p_N) p_1 - (M_{21} + M_{22} p_N)}{(M_{11} + M_{12} p_N) p_1 + (M_{21} + M_{22} p_N)},$$
$$t = \frac{2 p_1}{(M_{11} + M_{12} p_N) p_1 + (M_{21} + M_{22} p_N)}. \quad (1)$$

Then, reflectances and transmittances in case of TE and TM incident waves are calculated as [18]

$$R_{TE} = |r|^2\Big|_{q=1},\ T_{TE} = \frac{p_N}{p_1}|t|^2\Big|_{q=1}, \quad (2)$$

$$R_{TM} = |r|^2\Big|_{q=-1},\ T_{TM} = \frac{p_N}{p_1}|t|^2\Big|_{q=-1}. \quad (3)$$

Given that the polarization density of MUT is proportional to the projection of the electric field strength vector of incident EM wave on its surface, E_{MUT}, a bigger contrast between R_{TE} and R_{TM} values is expected for higher angles of incidence. Thus, we use the characteristic matrix technique to fit the reflection spectra measured for all MUT samples in the configurations of experimental setup №7 and №19.

When fitting empirical data by $R_{TE}(f, \epsilon_r, \tan\delta)$, we acquire a relative permittivity $\epsilon_r = 7.23$ and a loss tangent

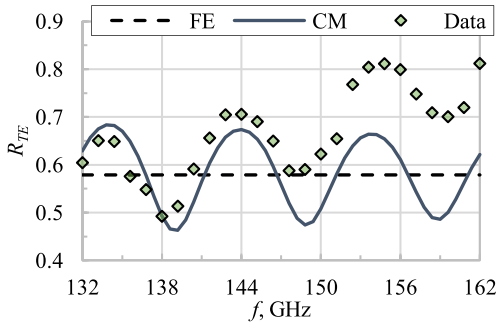

(a) Experimental setup in configuration №19.

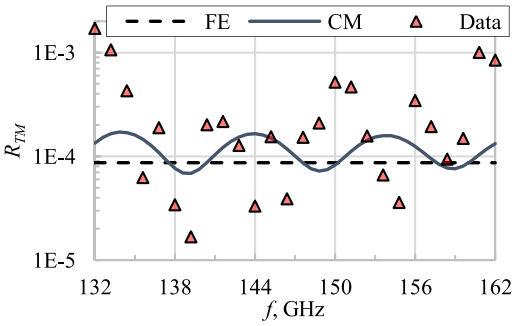

(b) Experimental setup in configuration №7.

FIGURE 6. Reflection spectra of a 6 mm thick plate glass sample. "FE" and "CM" denote calculations by Fresnel's equations and characteristic matrix technique, and "Data" denotes empirically acquired data.

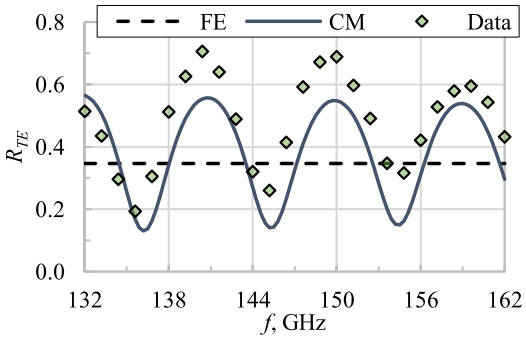

(a) Experimental setup in configuration №19.

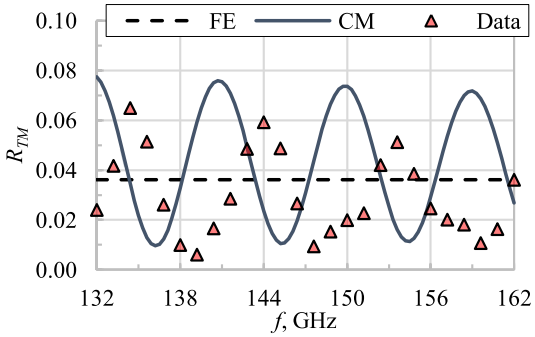

(b) Experimental setup in configuration №7.

FIGURE 7. Reflection spectra of a 12.5 mm thick drywall sample. "FE" and "CM" denote calculations by Fresnel's equations and characteristic matrix technique, and "Data" denotes empirically acquired data.

$\tan\delta = 0.03$ for the glass sample. These parameters are qualitatively consistent with those reported in the literature for a cover slip at sub-THz frequencies [19]. The data and the resulting fit function together with the prediction of Fresnel's equations are provided in Fig. 6(a). The observed offset of 0.05–0.1 between the CM fit and the measured R_{TE} values is due to a minor divergence of the Tx beam which is not accounted for in the definition of the characteristic matrix. Referring to Fig. 6(b), the beam divergence also results in a moderate deviation of the measured R_{TM} values from those predicted by the CM fit for TM incident wave. Moreover, the corresponding reflectance frequency profiles demonstrate notable similarity with an offset along the abscissa axis of a few gigahertz. This can be explained as follows. In contrast to a plane-parallel beam, MUT is illuminated by the central part of the Tx beam with non-constant amplitude and phase. And the very central ray is the only incident on the MUT surface at 70°. The angles of incidence of the other rays in the beam vary from approximately 60° to 80°. This results in significant changes of the corresponding E_{MUT} values and, consequently, in distortion of the interference pattern. None of the aforementioned effects are accounted for in Fresnel's equations, which demonstrate unacceptable accuracy for calculating reflectance for both TE and TM incident waves.

The same trends are observed for the drywall sample found to have $\epsilon_r = 2.63$, $\tan\delta = 0.01$. Fig. 7 demonstrates the corresponding reflection spectra acquired by measurements and calculations.

We also observe consistency between the predictions of the characteristic matrix technique and the data empirically acquired for other specular reception cases, when $\theta_1 = \theta_1'$, for both glass and drywall samples.

Regarding the aerated concrete sample, we first decide to investigate its porosity in order to develop a proper dielectric model. A pore diameter of 0.63±0.49 mm was statistically acquired for a confidence interval of 95%. Given that operating frequency ranges from 132 to 162 GHz, the mean pore size is noticeably less than the free space wavelength of the EM wave incident on the sample surface. To analyze measurement results, we consider our sample as a homogeneous medium with the effective relative permittivity, $\hat{\epsilon}_{eff}$, acquired within a general model of porous dielectrics [22]:

$$\hat{\epsilon}_{eff} = \hat{\epsilon}_r \left(1 + 3\phi \frac{1-\hat{\epsilon}_r}{1+3\hat{\epsilon}_r}\right)\left(1 - \phi \frac{1-\hat{\epsilon}_r}{1+3\hat{\epsilon}_r}\right)^{-1}. \quad (4)$$

Given that the measured porosity of the aerated concrete sample $\phi = 0.32 \pm 0.11$ and the interpolated complex permittivity of solid concrete $\hat{\epsilon}_r = 5.99 + 0.37i$ at 156 GHz [23], (4) provides better accuracy as compared to Maxwell-Garnett approximations [24]. We acquire $\hat{\epsilon}_{eff} = 4.13 + 0.23i$ and

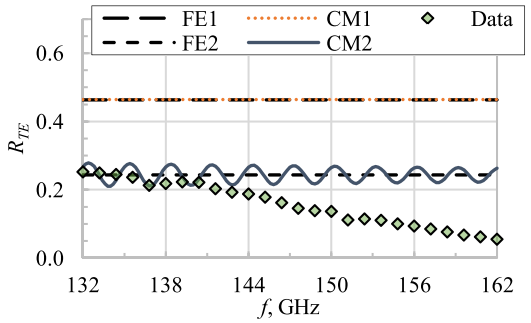

(a) Experimental setup in configuration №19.

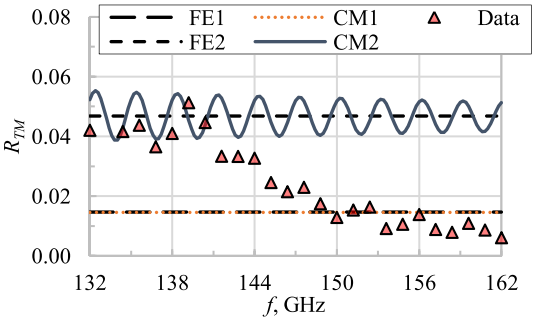

(b) Experimental setup in configuration №7.

FIGURE 8. Reflection spectra of a 50 mm thick concrete sample. "FE1", "FE2" and "CM1", "CM2" denote calculations by Fresnel's equations and characteristic matrix technique, and "Data" denotes empirically acquired data.

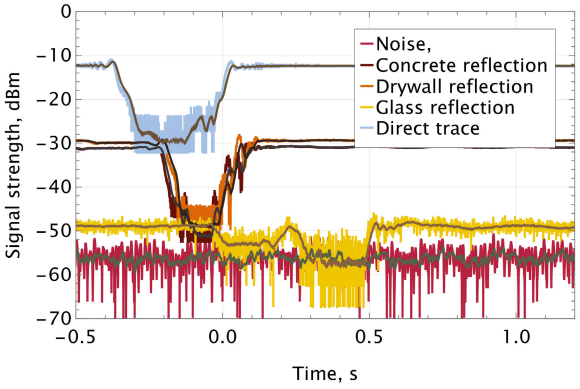

(a) E-plane of incidence (3 m LoS and setup №7 with MUT).

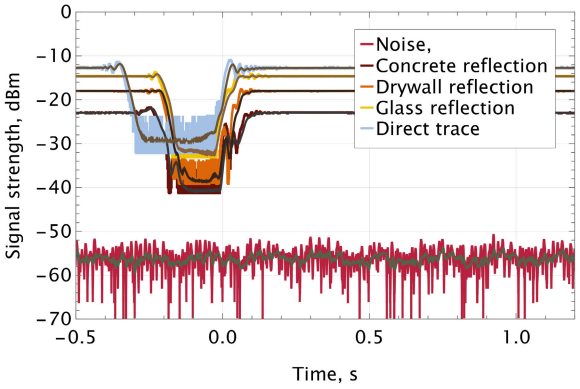

(b) H-plane of incidence (3 m LoS and setup №19 with MUT).

FIGURE 9. Received signal dynamics with blockage over LoS and in-reflection propagation paths.

substitute this value in (2) and (3), and Fresnel's equations. Fig. 8 provides the calculated reflection spectra, which are denoted as "CM1" and "FE1". The figure, in addition, provides the "CM2" and "FE2" fit functions to the experimental data. They are also acquired with the aid of (2) and (3), and Fresnel's equations, but for $\hat{\epsilon}_{eff} = 1.9 + 0.017i$. Solving (4) with respect to $\hat{\epsilon}_r$, we acquire a value of $2.4 + 0.027i$ intrinsic to a solid concrete material. This values are consistent with the measurement results for other specular reception cases. Moreover, the average root mean square error of the approximation decreases from 0.049–0.12 to 0.0029–0.0075 if $\theta_1 = \theta_1'$ are changed from 70° to 30–50°. In contrast to what one can observe in Fig. 8, this corresponds to the agreement between the resulting fit functions and empirical data not only up to 140 GHz, but over the entire frequency range of $132 - 162$ GHz. Given that propagation losses due to absorption and scattering obey the same exponential dependence, we do not distinguish their contribution in the imaginary part of the resulting permittivity of our porous sample.

V. BLOCKAGE LOSSES OF NLoS PROPAGATION PATHS

In this section, we investigate the excessive losses occurring in a sub-THz NLoS channel with a single reflection of radio signal from a static obstacle followed by its blockage by a person in motion, i.e., blockage losses. We start with the time series of the signal strengths measured for different reflecting materials and propagation paths. Then, we proceed to reporting mean blockage losses and, finally, conclude the section by demonstrating their cumulative distribution functions (CDFs).

A. TIME SERIES REPRESENTATION

We start with a time series representation of the radio signal blockage over the NLoS propagation paths, as demonstrated in Fig. 9, for all the considered types of materials and orientations of the Tx/Rx antennas. For comparison purposes, we also show the dynamics of blockage over the LoS path with similar optical length (denoted as "direct trace" in Fig. 9). By visually inspecting the presented data, one may notice that the received signal levels for in-reflection propagation paths in no-blockage condition are significantly lower as compared to those of LoS paths. This is attributed to the reflection losses detailed below. Furthermore, we observe differences in both blockage profiles and signal levels before/after the blockage event for horizontally and vertically oriented E-planes of Tx/Rx antennas (the H-planes are respectively orthogonal). The former condition is referred to as the E-plane of incidence (E-PoI), and the latter – as the H-plane of incidence (H-PoI). However, the visual inspection

does not allow one to highlight any difference between loss- and time-related blockage metrics for different materials thus requiring detailed statistical analysis.

B. IMPACT OF AoD AND AoR

To analyze the relevance of the empirically acquired signal strengths for clear and blocked propagation paths, we use the conventional log-distance path loss model relying on the Friis transmission formula along with the material-dependent reflection model formulated by us earlier in Section IV. Thus, path, $L_{p,P}$, and reflection losses, $L_{r,P}$, can be simulated in accordance with (5) and (6) for both TE and TM propagating waves. The term $I_P(\theta' - \theta)$, equal to the normalized Tx/Rx radiation intensity in decibels for a given pair of AoD and AoR, is introduced to account for the additional losses of the non-specular NLoS propagation paths arranged in experiments. Given that the Fraunhofer distance $F_d = 0.34$ m for the employed Tx/Rx antenna, we chose a reference distance $l_0 = 1$ m in all the simulations. The blockage losses are directly extracted from the measured time series as the difference in signal strengths for the non-blocked and blocked states of the channel. We has previously described the extraction procedure in details in [4].

$$L_{p,P}(x) = -2G_a + 20\log\left(\frac{4\pi f l_0}{c}\right) + 20\log\left(\frac{x}{l_0}\right) \tag{5}$$

$$L_{r,P}(\theta, \theta', \hat{\epsilon}_r) = -I_P(\theta' - \theta) - 10\log(R_P(\theta', \hat{\epsilon}_r)) \tag{6}$$

The results of the measurements statistical analysis and simulations of path, reflection and blockage losses are summarized in Table 2. For the convenience of the reader, it also highlights vital parameters of the experimental setup configurations detailed earlier in Table 1.

Our first critical conclusion is related to the impact of AoD and AoR. As one may observe, the results corresponding to the configurations with a (30, 70)° pair of angles are missing in Table 2. The rationale is that the received signal in the blocked state for these configurations is below the noise level for all the considered materials. This observation can be explained by the drastically enlarged contribution of the I_P term to the total loss in the channel. Moreover, the value of $-I_P(40°)$ reaches 49 dB for TE-polarized and 25 dB for TM-polarized signals. The observed trend is qualitatively in line with the results previously reported in [11] and [17] confirming that the received signal strength drastically diminishes with the increase in difference between AoD and AoR. On the other hand, for a 20° difference between the angles, the received signal is still detectable. Indeed, the $-I_P$ values are within 16–34 dB now. And the material-dependent part of the reflection loss is determined only by AoR in our experiments. We can evidently conclude that glass is a poor reflector as compared to concrete and drywall for TM-polarized radio signal and the pair of angles (70, 70)°: it adds to the channel 39 dB of intrinsic reflection loss. This is explained by its Brewster's angle of 69.6° which, in turn, leads to the reflection loss of just a 2 dB if the signal is TE-polarized. Drywall and concrete behave similarly, and their intrinsic reflection losses are within 5–15 dB. Moreover, for the (30, 30)° configurations, all the materials have comparable intrinsic reflection losses of 5–19 dB.

By analyzing the reported data further, one may observe that the orientation of the antennas polarization planes with respect to the plane of incidence greatly impacts on the received signal strength. This is consistent with the forecasts of the sample-defined reflection models described earlier in Section IV. And the asymmetry in the side lobe levels of the Tx and Rx antenna beams results in the additional losses ranging from 16 to 49 dB as measured for 3.55–4.3 m long non-specular paths with AoD and AoR within $30 - 70°$. The highest total losses are attributed to the E-PoI configurations potentially compromising measurement accuracy. To this aim, in what follows, we mainly concentrate on the H-PoI configurations.

Now, let us consider the mean blockage losses for different materials. First of all, we observe that while the antenna polarization plane orientation affects the received signal strength largely, its impact on the blockage loss values is rather limited. All the material samples reveal almost constant blockage losses of approximately 6–16 dB. However, the choice of the (AoD, AoR) configuration affects the mean blockage losses significantly. Specifically, the biggest impact is observed when the angles are equal, i.e., for specular paths corresponding to the (70, 70)°, (50, 50)° and (30, 30)° configurations. The blockage losses increase as the angles become smaller, that is, the blockage loss is higher by 2–6 dB for the (30, 30)° as compared to the (70, 70)° configurations. Please note, however, that this increase is compensated by lower reflection losses as compared to non-specular paths.

Further, we analyze the impact of reflecting material and Tx-Rx height. With respect to the former, one may observe that for the H-PoI configurations (i.e., the antennas orientation of interest) the mean blockage loss is less for glass as compared to other materials for both considered Tx-Rx heights by approximately 3–5 dB. Concrete, in turn, produces slightly smaller loss as compared to drywall but the difference is barely noticeable. By cross-comparing the results for a single material but different Tx-Rx heights, we observe the same expected trends – the mean loss is generally higher at 1.45 m height as compared to 1.65 m height. This is a geometry-defined effect since these heights correspond to the levels of the blocker's chest and head, respectively.

By comparing the obtained results with those reported in [4] for the LoS blockage scenarios with similar lengths of optical paths, one may deduce that the presence of a reflector results in quantitative changes in the blockage loss. Thus, depending on the reflecting material and (AoD, AoR), the mean blockage loss increases by 3–7 dB. It has to be kept in mind, however, that blocker-to-Rx distance is twice shorter.

TABLE 2. The mean path, reflection and blockage losses.

Material/ setup	Tx-Rx height	PoI	(AoD, AoR), °	Path, m	Rx signal, dBm (clear path)	Total loss, dB (measured)	Path loss, dB (simulated)	Reflection loss, dB (simulated)	Rx signal, dBm (blocked path)	Blockage loss, dB (measured)
Concrete/№1	Head	E	(70, 70)	3.00	-30.96	47.39	29.04	12.88	-40.67	9.71
Concrete/№4	Head	E	(50, 50)	3.00	-40.71	57.14	29.04	29.22	-49.94	9.23
Concrete/№6	Head	E	(30, 30)	3.00	-28.47	44.91	29.04	18.23	-42.76	14.29
Concrete/№7	Chest	E	(70, 70)	3.00	-30.96	47.40	29.04	12.88	-43.59	12.64
Concrete/№10	Chest	E	(50, 50)	3.00	-40.36	56.79	29.04	29.22	-50.92	10.55
Concrete/№12	Chest	E	(30, 30)	3.00	-28.49	44.93	29.04	18.23	-41.61	13.12
Concrete/№13	Head	H	(70, 70)	3.00	-23.13	39.56	29.04	5.79	-33.65	10.53
Concrete/№16	Head	H	(50, 50)	3.00	-24.74	41.17	29.04	10.41	-41.69	16.95
Concrete/№18	Head	H	(30, 30)	3.00	-26.76	43.20	29.04	14.26	-43.13	16.37
Concrete/№19	Chest	H	(70, 70)	3.00	-22.95	39.38	29.04	5.79	-35.04	12.09
Concrete/№22	Chest	H	(50, 50)	3.00	-24.71	41.14	29.04	10.41	-38.86	14.15
Concrete/№24	Chest	H	(30, 30)	3.00	-26.80	43.23	29.04	14.26	-41.60	14.80
Drywall/№1	Head	E	(70, 70)	3.00	-29.38	45.81	29.04	15.36	-40.78	11.40
Drywall/№4	Head	E	(50, 50)	3.00	-31.92	48.35	29.04	18.40	-43.21	11.28
Drywall/№5	Head	E	(30, 50)	3.55	-49.69	66.12	30.50	34.30	-56.34	6.65
Drywall/№6	Head	E	(30, 30)	3.00	-29.83	46.27	29.04	19.48	-44.66	14.83
Drywall/№7	Chest	E	(70, 70)	3.00	-29.44	45.88	29.04	15.36	-41.75	12.31
Drywall/№10	Chest	E	(50, 50)	3.00	-31.98	48.41	29.04	18.40	-45.08	13.10
Drywall/№12	Chest	E	(30, 30)	3.00	-29.81	46.25	29.04	19.48	-42.39	12.58
Drywall/№13	Head	H	(70, 70)	3.00	-18.01	34.44	29.04	5.06	-30.11	12.10
Drywall/№16	Head	H	(50, 50)	3.00	-19.65	36.08	29.04	5.78	-32.04	12.39
Drywall/№18	Head	H	(30, 30)	3.00	-24.89	41.33	29.04	16.02	-39.37	14.49
Drywall/№19	Chest	H	(70, 70)	3.00	-18.03	34.47	29.04	5.06	-31.55	13.52
Drywall/№22	Chest	H	(50, 50)	3.00	-19.63	36.07	29.04	5.78	-32.44	12.80
Drywall/№24	Chest	H	(30, 30)	3.00	-24.93	41.36	29.04	16.02	-38.30	13.37
Glass/№1	Head	E	(70, 70)	3.00	-48.49	64.92	29.04	39.03	-57.08	8.59
Glass/№4	Head	E	(50, 50)	3.00	-24.56	40.99	29.04	12.29	-34.63	10.07
Glass/№5	Head	E	(30, 50)	3.55	-45.69	62.12	30.50	28.19	-53.23	7.54
Glass/№6	Head	E	(30, 30)	3.00	-18.97	35.41	29.04	6.52	-33.42	14.45
Glass/№7	Chest	E	(70, 70)	3.00	-49.30	65.74	29.04	39.03	-55.62	6.33
Glass/№10	Chest	E	(50, 50)	3.00	-24.57	41.00	29.04	12.29	-36.93	12.35
Glass/№11	Chest	E	(30, 50)	3.55	-45.34	61.77	30.50	28.19	-52.98	7.64
Glass/№12	Chest	E	(30, 30)	3.00	-21.88	38.31	29.04	6.52	-33.01	11.13
Glass/№13	Head	H	(70, 70)	3.00	-14.66	31.09	29.04	2.14	-25.11	10.45
Glass/№14	Head	H	(50, 70)	4.30	-48.30	64.73	32.17	36.59	-54.78	6.48
Glass/№16	Head	H	(50, 50)	3.00	-18.29	34.73	29.04	5.45	-31.56	13.27
Glass/№18	Head	H	(30, 30)	3.00	-17.84	34.27	29.04	4.77	-32.49	14.65
Glass/№19	Chest	H	(70, 70)	3.00	-14.65	31.08	29.04	2.14	-26.14	11.49
Glass/№22	Chest	H	(50, 50)	3.00	-18.28	34.71	29.04	5.45	-31.22	12.93
Glass/№24	Chest	H	(30, 30)	3.00	-19.87	36.31	29.04	4.77	-33.24	13.37

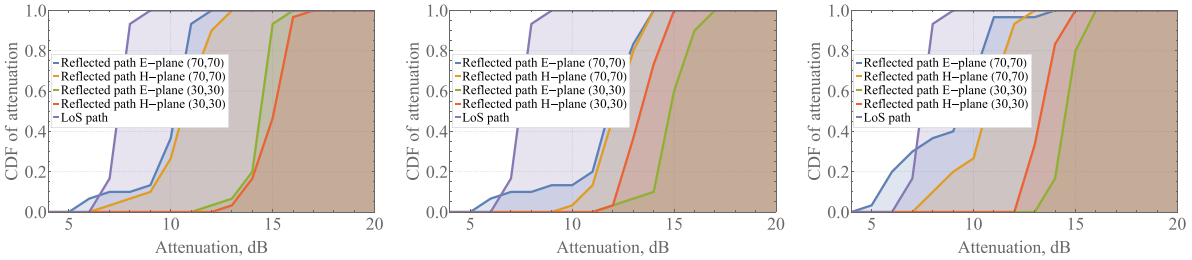

(a) Concrete (b) Drywall (c) Glass

FIGURE 10. CDF of blockage losses for LoS, specular paths with different PoI and (AoD, AoR).

C. DISTRIBUTIONS OF BLOCKAGE LOSSES

To provide additional information regarding the signal strength in the channel, Fig. 10 demonstrates CDFs of blockage losses for different cases. All the presented cases here correspond to the Tx-Rx path located at the height of 1.65 m, the results for a 1.45 m height are omitted as they exhibit similar behaviour.

Fig. 10 shows CDFs of blockage losses for different planes of incidence and the pairs of angles (AoD, AoR). We also complemented this illustration with the losses over the LoS path with the same optical length taken from [4]. It is evident from the figure that LoS-propagating signal experiences the least attenuation, closely followed by that of in-reflection propagation path with AoD and AoR of 70°, while the path with AoD and AoR of 30° demonstrates the highest attenuation. This is also consistent with the data in Table 2 and can be explained by Tx/Rx antennas radiation pattern and measurement geometry. Indeed, the area of the wavefront incident on reflecting material enlarges in response to increasing AoD. This results in a smaller overlap with blocker crossing reflected Tx beam and, in turn, reduces attenuation of radio signal.

Analyzing the data in Fig. 10 further, one may observe that the plots for E- and H-planes of incidence of radio signal are located quite close to each other, almost coinciding in case of concrete and drywall. Minor differences in case of glass can be attributed to external factors such as Rx dynamic range and consistency of blocker's trajectories of motion. The similarity in these data shows that while signal strength highly depends on the orientation of Tx/Rx antennas as was shown earlier in Fig. 9 and Table 2, it basically does not impact on blockage losses. Moreover, one can note that the reported blockage losses weakly depend on the choice of reflecting material too.

VI. BLOCKAGE TIMINGS OF NLoS PROPAGATION PATHS

In addition to attenuation statistics, time-related parameters of radio signal blockage are of high practical importance for the design of sub-THz communication systems. In this section, we report on blockage duration, signal fall and recovery times including their mean values and CDFs. Note that the signal recovery time is vital in the context of blockage detection [4], [25], while the blockage duration is critical for designing algorithms to improve service reliability.

A. MEAN BLOCKAGE TIMINGS

The mean values of the blockage duration, t_B, signal fall, t_F, and recovery times, t_R, for all the considered measurement configurations are reported in Table 3. Below, when discussing the major takeaways, we mainly concentrate on H-PoI configurations as they ensure the least total losses. The results for E-PoI configurations are also provided for completeness.

By analyzing the angular dependencies of the blockage duration, we observe that for both specular and non-specular paths, there are no straight forward trends in the considered metrics. In general, the mean blockage duration varies in the range of $250-350$ ms with infrequent outliers to 200 and 400 ms. The mean signal recovery and fall times for the PoI of interest are generally in the ranges of $40-70$ ms and $60-100$ ms, respectively. And the fall times are usually 1.5 times longer than the recovery times.

By cross-comparing the considered timing for different reflecting materials, one may observe that the mean values of the investigated metrics are also insensitive to the material choice. The evident input parameter noticeably affecting them is the Tx-Rx height. In general, its decrease results in longer mean blockage duration due to smaller overlap between the radio signal wave front and the blocker crossing the signal-carrying beam. The resulting difference is on the order of 10–30 ms on average. The mean signal fall and recovery times logically remain unaffected by the adjustment of the Tx-Rx height. It is also worth mentioning that some experimental setup configurations exhibit LoS signal delivery through the Tx/Rx antenna side lobes. This is characterized by the appearance of the additional blocked state in the measured time series of the Rx signal. Since the side lobe level at 20–40° relative to the antenna optical axis varies from −16 to −49 dB, this effect is pronounced only for the specular paths with (AoD, AoR) of (70, 70)°. And the signal strength attributed to it is at least 17 dB below the main radio signal component delivered upon reflection for concrete and drywall. For glass, however, the two components are almost equal in case of TM-polarized radio signals (see the corresponding glass reflection trace in Fig. 9).

Note that our observations are generally in line with the results for mean blockage duration, signal fall and recovery times reported in [4] for the LoS blockage scenarios. Specifically, reflection does not change these timings quantitatively implying that the blockage detection [4], [25] and avoidance techniques such as, e.g., multiconnectivity [26], should not be modified to handle reflection-aided sub-THz communications in indoor deployments.

TABLE 3. The mean blockage duration, signal fall and recovery times.

Setup	Tx-Rx height	PoI	(AoD, AoR), °	t_B, ms	t_R, ms	t_F, ms
Concrete						
№1	Head	E	(70, 70)	250.53	41.33	62.56
№4	Head	E	(50, 50)	325.90	33.05	25.36
№6	Head	E	(30, 30)	284.77	72.45	90.08
№7	Chest	E	(70, 70)	276.42	39.60	74.24
№10	Chest	E	(50, 50)	245.28	55.83	66.40
№12	Chest	E	(30, 30)	315.32	67.43	86.21
№13	Head	H	(70, 70)	306.34	42.71	90.08
№16	Head	H	(50, 50)	232.81	41.42	64.53
№18	Head	H	(30, 30)	289.32	46.42	61.21
№19	Chest	H	(70, 70)	276.42	39.60	74.24
№22	Chest	H	(50, 50)	326.42	42.39	54.16
№24	Chest	H	(30, 30)	398.23	77.32	86.32
Drywall						
№1	Head	E	(70, 70)	326.45	48.55	45.99
№4	Head	E	(50, 50)	216.03	33.87	39.43
№5	Head	E	(30, 50)	301.73	48.32	76.00
№6	Head	E	(30, 30)	235.04	49.87	56.16
№7	Chest	E	(70, 70)	234.05	46.36	55.17
№10	Chest	E	(50, 50)	264.32	23.35	37.64
№12	Chest	E	(30, 30)	284.77	73.31	61.87
№13	Head	H	(70, 70)	314.12	48.37	63.61
№16	Head	H	(50, 50)	306.12	65.12	87.25
№18	Head	H	(30, 30)	313.23	65.21	79.67
№19	Chest	H	(70, 70)	314.12	48.37	63.61
№22	Chest	H	(50, 50)	314.32	37.57	67.78
№24	Chest	H	(30, 30)	298.12	34.13	48.37
Glass						
№1	Head	E	(70, 70)	239.87	47.44	49.81
№4	Head	E	(50, 50)	203.24	42.81	37.61
№5	Head	E	(30, 50)	198.81	30.40	37.13
№6	Head	E	(30, 30)	206.12	34.01	43.23
№7	Chest	E	(70, 70)	265.73	26.22	2.32
№10	Chest	E	(50, 50)	276.12	39.31	52.83
№11	Chest	E	(30, 50)	224.12	60.34	53.23
№12	Chest	E	(30, 30)	277.99	72.45	39.86
№13	Head	H	(70, 70)	275.79	47.45	84.77
№14	Head	H	(50, 70)	324.12	23.24	36.25
№16	Head	H	(50, 50)	203.12	23.12	46.64
№18	Head	H	(30, 30)	277.95	72.45	39.86
№19	Chest	H	(70, 70)	275.79	47.45	84.77
№22	Chest	H	(50, 50)	231.01	39.56	46.61
№24	Chest	H	(30, 30)	277.95	72.45	39.86

B. DISTRIBUTIONS OF BLOCKAGE TIMINGS

Complementing the mean values, we also present the CDFs of blockage duration, signal fall and recovery times in Fig. 11–13. All the presented data here correspond to the

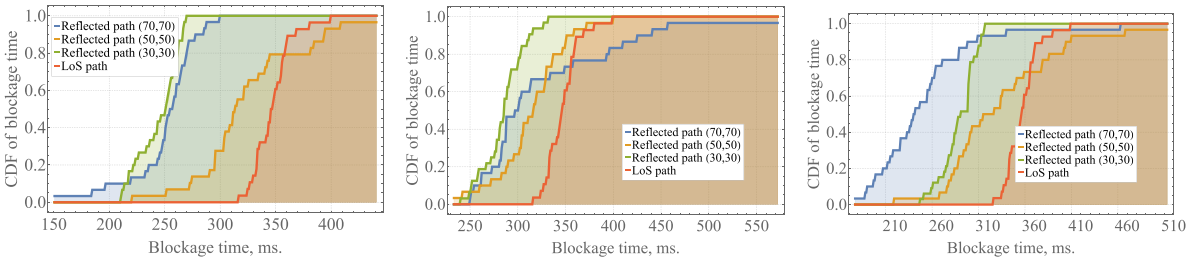

(a) Concrete (b) Drywall (c) Glass

FIGURE 11. CDF of blockage durations for LoS, specular paths with a 1.65 m Tx/Rx height, H-PoI and different (AoD, AoR).

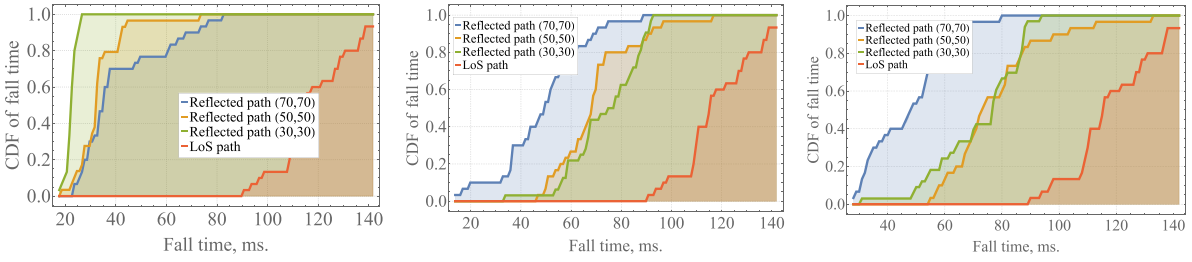

(a) Concrete (b) Drywall (c) Glass

FIGURE 12. CDF of signal fall times for LoS, specular paths with a 1.65 m Tx/Rx height, H-PoI and different (AoD, AoR).

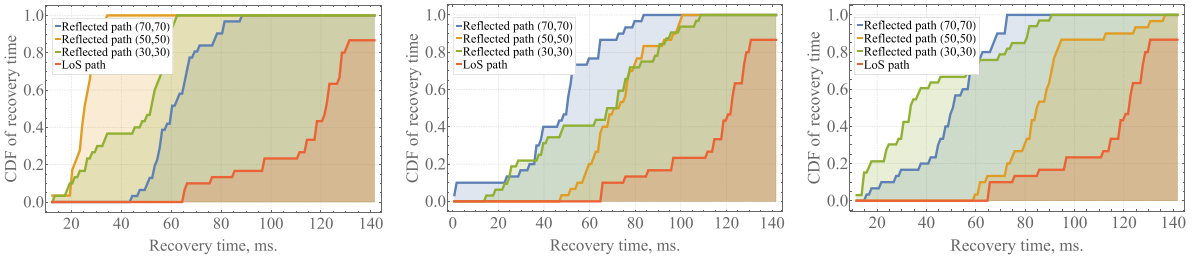

(a) Concrete (b) Drywall (c) Glass

FIGURE 13. CDF of signal recovery times for LoS, specular paths with a 1.65 m Tx/Rx height, H-PoI and different (AoD, AoR).

Tx/Rx height of 1.65 m and the H-PoI of radio signal; the results for a 1.45 m height and E-PoI are omitted as they exhibit similar behaviour. In all thee figures, we also show the corresponding CDFs for the LoS paths with similar optical lengths taken from [4].

By analyzing the time-related metrics of specular paths provided in Fig. 11, we observe that they are characterized by slightly smaller blockage duration as compared to LoS paths. In general, the CDF of blockage duration over LoS path has a steeper behavior which is especially pronounced for (AoD, AoR) of $(70, 70)^\circ$ and $(50, 50)^\circ$. This can be attributed to higher variance in blockage duration caused by the diffraction effects discussed earlier in Section IV. By cross-comparing the blockage duration over specular paths for different materials, we also observe that drywall and glass are characterized by higher variance as compared to concrete.

By analyzing the signal fall and recovery times shown in Fig. 12 and Fig. 13, we observe that they are much shorter as compared to these metrics of the LoS paths. In practice, it implies that time-budget for blockage detection is much smaller for reflection-aided propagation of radio signal. It reduces from approximately 80–100 ms intrinsic to LoS paths to just 20–40 ms for reflections from concrete and to 30–60 ms for reflections from drywall and glass. Similarly to the blockage duration CDFs, concrete is characterized by steeper form of the fall and recovery times CDFs as compared to drywall and glass.

VII. CONCLUSION

Most of the traffic in 6G sub-THz cellular systems is expected to originate indoors, where the link distances are generally shorter while reflection-aided communications are more common as compared to outdoor deployments. In this paper we characterized the impact of dynamic human body blockage over in-reflection propagation path on the signal strength for a highly directive indoor sub-THz channel. To this aim, we conducted a measurement campaign at the carrier frequency of 156 GHz and report on the reflection and blockage losses over various propagation paths as well as the corresponding blockage duration, signal fall and recovery times.

Our main findings are: (i) the complex permittivities of widely used construction materials such as flat glass, drywall and aerated concrete are equal to $7.23 + 0.22i$, $2.63 + 0.026i$,

$1.9 + 0.017i$, respectively; (ii) the reflection losses reach 16 dB for TE-polarized and 39 dB for TM-polarized radio signals; (iii) the path losses due to the asymmetry in the side lobe levels of the Tx and Rx antenna beams with 6° wide symmetric main lobes vary from 16 to 49 dB as measured for 3.55–4.3 m long non-specular propagation paths with AoD and AoR within $30 - 70°$; (iv) the blockage losses are in the range of $6 - 17$ dB, and their mean value is nearly unaffected by the choice of reflecting material in the propagation path; (v) the blockage duration, signal fall and recovery times are noticeably smaller than in the LoS channels with the same directivity, and the time-budget for blockage detection is 20–40 ms, i.e., 2–4 times as small as compared to the LoS propagation paths.

We can conclude that the dynamic blockage of radio signal in reflection-aided channels is statistically similar to that in the LoS channels, and the development of special communication algorithms is not required. The only exception is that the time-budget for blockage detection becomes much smaller: it reduces from approximately 80–100 ms to just 20–40 ms attributed to reflection-aided communications.

REFERENCES

[1] A. Zaidi, F. Athley, J. Medbo, U. Gustavsson, G. Durisi, and X. Chen, *5G Physical Layer: Principles, Models and Technology Components*. New York, NY, USA: Academic, 2018.

[2] M. Matthaiou, O. Yurduseven, H. Q. Ngo, D. Morales-Jimenez, S. L. Cotton, and V. F. Fusco, "The road to 6G: Ten physical layer challenges for communications engineers," *IEEE Commun. Mag.*, vol. 59, no. 1, pp. 64–69, Jan. 2021.

[3] D. Moltchanov, E. Sopin, V. Begishev, A. Samuylov, Y. Koucheryavy, and K. Samouylov, "A tutorial on mathematical modeling of 5G/6G millimeter wave and terahertz cellular systems," *IEEE Commun. Surveys Tuts.*, vol. 24, no. 2, pp. 1072–1116, 2nd Quart., 2022.

[4] A. Shurakov, D. Moltchanov, A. Prikhodko, A. Khakimov, E. Mokrov, V. Begishev, I. Belikov, Y. Koucheryavy, and G. Gol'tsman, "Empirical blockage characterization and detection in indoor sub-THz communications," *Comput. Commun.*, vol. 201, pp. 48–58, Mar. 2023.

[5] S. Nie, G. R. MacCartney, S. Sun, and T. S. Rappaport, "72 GHz millimeter wave indoor measurements for wireless and backhaul communications," in *Proc. IEEE 24th Annu. Int. Symp. Pers., Indoor, Mobile Radio Commun. (PIMRC)*, Sep. 2013, pp. 2429–2433.

[6] G. R. MacCartney, T. S. Rappaport, and S. Rangan, "Rapid fading due to human blockage in pedestrian crowds at 5G millimeter-wave frequencies," in *Proc. IEEE Global Commun. Conf.*, Dec. 2017, pp. 1–7.

[7] Y. Xing and T. S. Rappaport, "Propagation measurement system and approach at 140 GHz-moving to 6G and above 100 GHz," in *Proc. IEEE Global Commun. Conf. (GLOBECOM)*, Dec. 2018, pp. 1–6.

[8] J. M. Eckhardt, V. Petrov, D. Moltchanov, Y. Koucheryavy, and T. Kürner, "Channel measurements and modeling for low-terahertz band vehicular communications," *IEEE J. Sel. Areas Commun.*, vol. 39, no. 6, pp. 1590–1603, Jun. 2021.

[9] V. Petrov, J. M. Eckhardt, D. Moltchanov, Y. Koucheryavy, and T. Kurner, "Measurements of reflection and penetration losses in low terahertz band vehicular communications," in *Proc. 14th Eur. Conf. Antennas Propag. (EuCAP)*, Mar. 2020, pp. 1–5.

[10] K. Du, O. Ozdemir, F. Erden, and I. Guvenc, "Sub-terahertz and mmWave penetration loss measurements for indoor environments," 2021, *arXiv:2103.02745*.

[11] J. Kokkoniemi, J. Lehtomäki, V. Petrov, D. Moltchanov, and M. Juntti, "Frequency domain penetration loss in the terahertz band," in *Proc. Global Symp. Millim. Waves (GSMM) ESA Workshop Millimetre-Wave Technol. Appl.*, Jun. 2016, pp. 1–4.

[12] B. A. Bilgin, H. Ramezani, and O. B. Akan, "Human blockage model for indoor terahertz band communication," in *Proc. IEEE Int. Conf. Commun. Workshops (ICC Workshops)*, May 2019, pp. 1–6.

[13] Y. Wu, J. Kokkoniemi, C. Han, and M. Juntti, "Interference and coverage analysis for terahertz networks with indoor blockage effects and line-of-sight access point association," *IEEE Trans. Wireless Commun.*, vol. 20, no. 3, pp. 1472–1486, Mar. 2021.

[14] A. Shafie, N. Yang, S. Durrani, X. Zhou, C. Han, and M. Juntti, "Coverage analysis for 3D terahertz communication systems," *IEEE J. Sel. Areas Commun.*, vol. 39, no. 6, pp. 1817–1832, Jun. 2021.

[15] D. Moltchanov, Y. Gaidamaka, D. Ostrikova, V. Beschastnyi, Y. Koucheryavy, and K. Samouylov, "Ergodic outage and capacity of terahertz systems under micromobility and blockage impairments," *IEEE Trans. Wireless Commun.*, vol. 21, no. 5, pp. 3024–3039, May 2022.

[16] J. Kokkoniemi, V. Petrov, D. Moltchanov, J. Lehtomaeki, Y. Koucheryavy, and M. Juntti, "Wideband terahertz band reflection and diffuse scattering measurements for beyond 5G indoor wireless networks," in *Proc. Eur. Wireless ; 22th Eur. Wireless Conf.*, May 2016, pp. 1–6.

[17] I. Gaspard, "Co-and crosspolar scattering measurements at slightly rough walls for indoor propagation channels at mmWaves," in *Proc. IEEE-APS Topical Conf. Antennas Propag. Wireless Commun. (APWC)*, Sep. 2019, pp. 38–41.

[18] M. Born and E. Wolf, *Principles of Optics: Electromagnetic Theory of Propagation, Interference and Diffraction of Light*. Amsterdam, The Netherlands: Elsevier, 2013.

[19] J. W. Lamb, "Miscellaneous data on materials for millimetre and submillimetre optics," *Int. J. Infr. Millim. Waves*, vol. 17, no. 12, pp. 1997–2034, Dec. 1996.

[20] M. Naftaly and R. E. Miles, "Terahertz time-domain spectroscopy of silicate glasses and the relationship to material properties," *J. Appl. Phys.*, vol. 102, no. 4, Aug. 2007, Art. no. 043517.

[21] Y. Banday, G. Mohammad Rather, and G. R. Begh, "Effect of atmospheric absorption on millimetre wave frequencies for 5G cellular networks," *IET Commun.*, vol. 13, no. 3, pp. 265–270, Feb. 2019.

[22] X.-D. Liu, Z.-L. Hou, B.-X. Zhang, K.-T. Zhan, P. He, K.-L. Zhang, and W.-L. Song, "A general model of dielectric constant for porous materials," *Appl. Phys. Lett.*, vol. 108, no. 10, pp. 1–10, Mar. 2016.

[23] M. Urahashi and A. Hirata, "Complex permittivity evaluation of building materials at 200–500 GHz using THz-TDS," in *Proc. Int. Symp. Antennas Propag. (ISAP)*, Jan. 2021, pp. 539–540.

[24] T. C. Choy, *Effective Medium Theory: Principles and Applications*, vol. 165. Oxford Univ. Press, 2015.

[25] S. Wu, M. Alrabeiah, A. Hredzak, C. Chakrabarti, and A. Alkhateeb, "Deep learning for moving blockage prediction using real mmWave measurements," in *Proc. IEEE Int. Conf. Commun.*, May 2022, pp. 3753–3758.

[26] *NR; Multi-Connectivity; Stage 2 (Release 16)*, 3GPP, document TS 37.340 V16.0.0, Dec. 2019.

ALEXANDER SHURAKOV received the Specialist degree in physics and computer science from the Vyatka State University of Humanities, Russia, and the Ph.D. degree in radiophysics from the Kotelnikov Institute of Radioengineering and Electronics, Russian Academy of Sciences, in 2019.

In 2008, he joined the Radiophysics Laboratory, Moscow Pedagogical State University, Moscow, Russia, as a Graduate Student. In 2010, he qualified for a fellowship program with the Harvard-Smithsonian Center for Astrophysics, where he continued to work on cryogenic heterodyne receivers for radio astronomy, until 2013. He is currently an Associate Professor with the Department of General and Experimental Physics, Moscow Pedagogical State University, and a Senior Researcher with the Department of Quantum Optics and Telecommunications, HSE University, Moscow. He has coauthored dozens of scientific papers on super- and semiconductor electronic and radio-photonic circuits for terahertz remote sensing and sub-terahertz wireless communications. He has been a principal investigator and key implementer of numerous scientific projects in the aforementioned research areas. In 2021, he was awarded a stipend from the Ministry of Industry and Trade of the Russian Federation for the significant contribution to the development of terahertz devices and systems.

POLINA ROZHKOVA is currently pursuing the B.S. degree in fundamental physics with the Institute of Physics, Technology and Information Systems, Moscow Pedagogical State University, Moscow, Russia.

She is currently a Junior Research Assistant with the Laboratory of Quantum Detectors, Moscow Pedagogical State University. Her research interests include terahertz metrology, design and prototyping of microwave circuits, and sub-terahertz 6G wireless communications.

ABDUKODIR KHAKIMOV received the Ph.D. degree from the St. Petersburg State University of Telecommunications, in 2022, where he is currently pursuing the degree. Since 2019, he has been a Junior Researcher with the Institute of Applied Mathematics and Telecommunications, Peoples' Friendship University of Russia (RUDN University). He is engaged in research on access and core technologies for 5G and 5G+ networks. In particular, the integration of MEC technology into distributed computing networks.

EVGENY MOKROV received the B.S. and M.S. degrees in applied mathematics and informatics from the Peoples' Friendship University of Russia (RUDN University), Moscow, Russia, in 2012 and 2015, respectively, and the Ph.D. degree in candidate of physical and mathematical sciences, in 2019. He is currently a Senior Lecturer with RUDN University. His research interests include mathematical modeling, numerical analysis, queuing models, and wireless communication networks.

ANATOLIY PRIKHODKO received the B.S. degree in fundamental physics and the M.S. degree in physics and technology of nanostructures and nanomaterials from Moscow Pedagogical State University, Moscow, Russia, in 2017 and 2019, respectively. He is currently pursuing the Ph.D. degree in electronic engineering and communication systems with HSE University, Moscow.

He is a Junior Researcher with Moscow Pedagogical State University and the National Research University Higher School of Economics. His research interests include microwave and terahertz metrology, modeling, optimization, integration of Schottky diodes for terahertz applications, and terahertz 6G wireless communications.

VYACHESLAV BEGISHEV received the degree in applied mathematics and the candidate degree in physical and mathematical sciences from the Peoples' Friendship University of Russia (RUDN University), in 2016 and 2019, respectively. He is currently an Assistant Professor with the Department of Probability Theory and Cyber Security, RUDN University. He is also taking part in joint research projects between RUDN University and the Tampere University of Technology, being involved in the performance analysis of 5G/6G wireless networks. He is the author of more than 45 scientific publications on topics related to areas of study of 5G wireless communication networks analysis of the quality of service, performance evaluation of wireless networks with enabled D2D communications, and mmWave band communications.

YEVGENI KOUCHERYAVY received the Ph.D. degree from the Tampere University of Technology, Tampere, Finland, in 2004. He has authored numerous publications in the field of advanced wired and wireless networking and communications. His current research interests include various aspects of heterogeneous wireless communication networks and systems, and emerging communication technologies for digitally augmented future beings.

MIKHAIL KOMAROV (Senior Member, IEEE) is currently a Professor with the Department of Business Informatics, Graduate School of Business, HSE University. He is a specialist in wireless data transmission and IT. He is the Vice-Chair of the Special Interest Group on IoT with the Internet Society.

GREGORY GOL'TSMAN received the Ph.D. degree in physics of semiconductors from Moscow Pedagogical State University, Moscow, Russia, in 1973.

He is currently a Professor and the Chair of the Department of General and Experimental Physics, Moscow Pedagogical State University, and the Department of Quantum Optics and Telecommunication, HSE University, Moscow. He is a Pioneering Physicist. His past achievements include: the first observation of optical transitions between energy levels of excitons in monocrystalline semiconductors; the discovery of the negatively charged state of shallow donors and the positively charged state of shallow acceptors in monocrystalline semiconductors; the study of electronic energy relaxation in disordered films of superconductors; the discovery and promotion of the superconducting hot electron bolometric mixer; and the superconducting single-photon detector. He has won several prizes, including the stipend from the Soros Foundation for Professors, from 1996 to 2001, the IEEE Van Duzer Prize in Applied Superconductivity, in 2010, and the IEEE Award for Continuing and Significant Contributions in the Field of Applied Superconductivity, in 2017. In 2005, he founded a start-up company called Scontel, which produces ready-to-use superconducting receivers for near and far-infrared wavelengths. In 2015, an innovative company named TIRPhotonics LLC was established within the Skolkovo Foundation. This company develops and manufactures optical integrated chips (including quantum chips) for modern scientific experiments and instruments.